Geoderma 381 (2021) 114681

Contents lists available at ScienceDirect

Geoderma

journal homepage: www.elsevier.com/locate/geoderma

Microspectroscopy reveals dust-derived apatite grains in acidic, highly-weathered Hawaiian soils

Christian Vogel[a,1], Julian Helfenstein[b,c,*,1], Michael S. Massey[d,e,2], Ryo Sekine[f,g], Ruben Kretzschmar[h], Luo Beiping[i], Thomas Peter[i], Oliver A. Chadwick[j], Federica Tamburini[b], Camille Rivard[k,l], Hannes Herzel[a], Christian Adam[a], Ana E. Pradas del Real[m,n,2], Hiram Castillo-Michel[m], Lucia Zuin[o], Dongniu Wang[o], Roberto Félix[p], Benedikt Lassalle-Kaiser[l], Emmanuel Frossard[b]

[a] Bundesanstalt für Materialforschung und –prüfung (BAM), Unter den Eichen 87, 12205 Berlin, Germany
[b] Institute of Agricultural Sciences, ETH Zurich, 8315 Lindau, Switzerland
[c] Agroscope, 8046 Zürich, Switzerland
[d] Department of Earth and Environmental Sciences, California State University East Bay, Hayward, CA 94542, USA
[e] Environment Canterbury, Christchurch 8140, New Zealand
[f] UK Centre for Ecology and Hydrology, Benson Lane, Crowmarsh Gifford, Wallingford, Oxfordshire OX10 8BB, United Kingdom
[g] School of Science and Engineering, University of the Sunshine Coast, Moreton Bay Campus, Petrie, QLD 4502 Australia
[h] Institute of Biogeochemistry and Pollutant Dynamics, CHN, ETH Zürich, 8092 Zürich, Switzerland
[i] Center for Climate Systems Modeling, ETH Zürich, 8092 Zürich, Switzerland
[j] Department of Geography, University of California, Santa Barbara, CA 93106, USA
[k] TRANSFORM, INRAE, 44000 Nantes, France
[l] Synchrotron SOLEIL, Saint-Aubin, 91192 Gif-sur-Yvette, France
[m] ESRF—The European Synchrotron, ID21 beamline, 71 Avenue des Martyrs, 38000 Grenoble, France
[n] Madrid Institute for Agricultural Research (IMIDRA), N-II km 38,200, 28800 Alcala de Henares, Spain
[o] Canadian Light Source, 44 Innovation Boulevard, Saskatoon, SK S7N 2V3, Canada
[p] Helmholtz-Zentrum Berlin für Materialien und Energie GmbH, Albert-Einstein-Straße 15, 12489 Berlin, Germany

ARTICLE INFO

Handling Editor: Yvan Capowiez

Keywords:
Phosphorus transformations
Soil development
Aeolian dust inputs
P *K*-edge X-ray absorption spectroscopy
micro-Raman spectroscopy

ABSTRACT

Dust deposition is an important source of phosphorus (P) to many ecosystems. However, there is little evidence of dust-derived P-containing minerals in soils. Here we studied P forms along a well-described climatic gradient on Hawaii, which is also a dust deposition gradient. Soil mineralogy and soil P forms from six sites along the climatic gradient were analyzed with bulk (X-ray diffraction and P *K*-edge X-ray absorption near edge structure) and microscale (X-ray fluorescence, P *K*-edge X-ray absorption near edge structure, and Raman) analysis methods. In the wettest soils, apatite grains ranging from 5 to 30 μm in size were co-located at the micro-scale with quartz, a known continental dust indicator suggesting recent atmospheric deposition. In addition to co-location with quartz, further evidence of dust-derived P included backward trajectory modeling indicating that dust particles could be brought to Hawaii from the major global dust-loading areas in central Asia and northern Africa. Although it is not certain whether the individual observed apatite grains were derived from long-distance transport of dust, or from local dust sources such as volcanic ash or windblown fertilizer, these observations offer direct evidence that P-containing minerals have reached surface layers of highly-weathered grassland soils through atmospheric deposition.

1. Introduction

Phosphorus (P) is an essential element for all forms of life, and P availability is thus an important driver of ecosystem function and productivity (Westheimer, 1987). Phosphorus enters the terrestrial biosphere through soils, and the availability of P in soils is largely a

* Corresponding author.
E-mail address: julian.helfenstein@agroscope.admin.ch (J. Helfenstein).
[1] These authors contributed equally to this work.
[2] Present address.

https://doi.org/10.1016/j.geoderma.2020.114681
Received 11 June 2020; Received in revised form 7 August 2020; Accepted 11 August 2020
Available online 30 August 2020
0016-7061/ © 2020 The Authors. Published by Elsevier B.V. This is an open access article under the CC BY license (http://creativecommons.org/licenses/by/4.0/).

function of its chemical form. In unmanaged ecosystems, P is released to soils by the weathering of apatite (e.g. fluoroapatite: $Ca_{10}(PO_4)_6F_2$) from parent material, and is then incorporated into organic matter, adsorbed to soil particles, or precipitated as secondary phosphate minerals (Walker and Syers, 1976). In highly weathered soils, apatite from the parent material has been dissolved, and P is chiefly found in organic forms or associated with aluminum and iron oxides (Helfenstein et al., 2018; Prietzel et al., 2013).

Along with weathering of underlying rock, aeolian dust may provide a significant P input to unmanaged ecosystems (Bristow et al., 2010; Swap et al., 1992). The major global origins of dust are the deserts of Africa, the Middle East, and central Asia (Rea, 1994; Wiacek et al., 2010). For example, Bristow et al. (2010) calculated that approximately 22 Mt of dust are imported from the Sahara Desert to the Amazon Basin annually. Based on the amount of P in the dust from dust traps (0.59–0.94 g P kg^{-1} dust), the average P input in the Amazon Basin is around 0.12–0.42 kg P ha^{-1} yr^{-1} (Bristow et al., 2010), which in strongly weathered soils may exceed the annual resupply of available P from continued weathering (Chadwick et al., 1999). In recent decades, atmospheric P loading has increased due to increased combustion of fossil fuels and land cover change (Wang et al., 2015). Though it is well known that P from dust may play an important role in ecosystem productivity (Chadwick et al., 1999; Eger et al., 2013; Gu et al., 2019; Okin et al., 2004), apatite dust has not been directly observed in highly-weathered soil environments, from which parent material-derived apatite has weathered away.

The Kohala climatic gradient on the Hawaii archipelago provides a steep gradient in mean annual rainfall from 250 to 3200 mm, while other state factors such as parent material and age remain similar (Chadwick et al., 2003; Vitousek and Chadwick, 2013). On this 150,000 year old lava flow, soils have developed into a wide range of soil types ranging from near-neutral pH soils retaining characteristics of the parent material on the arid end, to highly-weathered, acidic, organic matter-rich soils on the humid end (Chadwick et al., 2003; Helfenstein et al., 2018). Since most atmospheric dust is deposited through rain (Jackson et al., 1971), the climatic gradient also represents a dust input gradient, with the highest dust inputs on the wet end of the gradient (Kurtz et al., 2001; Porder et al., 2007).

The development and application of spectroscopic methods (X-ray absorption near edge structure (XANES) spectroscopy, infrared spectroscopy, Raman spectroscopy, and ^{31}P nuclear magnetic resonance (NMR) spectroscopy) provide powerful alternatives to chemical extraction methods commonly used to study inorganic and organic soil P compounds (Doolette and Smernik, 2011; Hesterberg, 2010; Kizewski et al., 2011; Kruse et al., 2015; Vogel et al., 2016). However, spectroscopic techniques have limitations arising from detection limit issues, spectral similarities between P bonding environments despite differing molecular structures, and various methodological limitations unique to each individual approach (Kruse et al., 2015). Consequently, detection and identification of P forms in soils using bulk spectroscopic techniques has been limited to describing general trends such as shifts from calcium associated P (Ca-P) to aluminum associated P (Al-P) or iron associated P (Fe-P) (Eriksson et al., 2016; Prietzel et al., 2013). However, micro-spectroscopy approaches have the potential to identify individual P forms that may be masked in a bulk spectrum, as well as to study the spatial co-location of P forms in relation to other elements and soil minerals. For example, micro-XANES coupled with microscale X-ray fluorescence (micro-XRF) can be used to probe P forms while preserving soil physical structure and allowing direct observation of associations with elements such as Al and Ca (Lombi et al., 2006; Rivard et al., 2016; Vogel et al., 2016, 2018; Liu et al., 2017; Werner et al., 2017; Hesterberg et al., 2017; Adediran et al., 2020). Also, micro-Raman spectroscopy is able to identify both apatite and quartz (Vogel et al., 2013); the latter is an established dust-derived mineral not present in parent material on Hawaii. Hence these two micro-spectroscopic techniques could help reveal the importance of dust-derived apatite in soil.

The aim of this study was to identify P species across a climate and dust input gradient, by evaluating bulk- and microscale P speciation. Particular attention was given to contrasts between A (surface) and B (subsurface) soil horizons to provide a better understanding of aeolian P input to Hawaiian ecosystems. First, we analyzed soil mineralogy and bulk soil P speciation. Second, we performed microscale P *K*-edge XANES (micro-XANES) to identify P forms in relation to other elements (Al and Ca), and to determine if micro-spectroscopy reveals apatite grains not apparent in bulk spectra. Thirdly, micro-Raman spectroscopy was used to identify collocated quartz and apatite, as evidence for a dust deposition layer. And lastly, we used the micro-spectroscopic data to parametrize a dust transport and deposition model, in order to calculate backward trajectories of trans-continental dust particles and speculate on the provenance of dust found on Hawaii.

2. Materials and methods

2.1. Site description, soil sampling, and soil analysis

The soils along the Kohala climatic gradient have been extensively described in previous works (Chadwick et al., 2003; Helfenstein et al., 2018; Vitousek and Chadwick, 2013; Siegenthaler et al., 2020). In brief, mean annual precipitation on the leeward side of the Kohala volcano increases from around 250 mm at the coast to around 3200 mm at circa 1060 m above sea level (Giambelluca et al., 2013). Though the climate gradient also has a temperature component (since temperature decreases with increased elevation), precipitation is the primary driver of soil processes and microbial and plant community structure along the climosequence (Chadwick et al., 2003; Peay et al., 2017; Vitousek and Chadwick, 2013). Samples of soil A and B horizons were taken from six sites in three soil process domains, as described by Vitousek and Chadwick (2013), along the Hawi lava flow on the Kohala volcano, Hawaii. Two sites were in an arid climate regime (sites 1 and 2, with 275 and 316 mm mean annual precipitation), while two were in an intermediate, subhumid climate regime with dry and wet cycles (sites 3 and 4, with 1340 and 1578 mm mean annual precipitation). Finally, samples were taken from two mostly humid sites (sites 5 and 6, with 2163 and 3123 mm mean annual precipitation). Further sampling details are discussed in Helfenstein et al. (2018), and additional information on the sites can be found in Table S1. Soils at the arid sites (1 and 2) are classified as Clayey-skeletal, isotic, isohyperthermic Sodic Haplocambids or medial-skeletal, ferrihydritic, isohyperthermic Typic Haplotorrands, depending on the exact values of density, oxalate extractable Fe and Al, and P sorption parameters (see Chadwick et al. (2003) for details). Soils at subhumid sites (3 and 4) are classified as medial, ferrihydritic, isothermic Andic Haplustolls or medial, amorphic, isomesic Humic Haplustands, depending on the expression of a Mollic epipedon and Andic properties. Soils at humid site 5 are classified as Medial, amorphic, isomesic Hydric Fulvudands, and those at humid site 6 are classified as Medial, amorphic, isomesic Hydric Fulvudands and Alic Epiaquands, depending on subtle differences in landscape curvature. In addition, fresh parent material samples were taken from a roadsite cut on the arid end of the climate gradient.

Soil pH was measured in water using a soil:solution ratio of 1:2.5 and 24-h equilibration time (FAL et al., 1996). Total C and N were measured on bulk soil samples with an elemental analyzer (Vario Pyro Cube, Elementar GmbH, Hanau, Germany). The total contents of P, Si, Al, Fe, Ca were analyzed by energy-dispersive X-ray fluorescence spectrometry (XRF; XEPOS, Spectro, Kleve, Germany) using pellets prepared from 4 g of soil and 0.9 g of an amide wax (N,N′-Bisstearoylethylenediamide, Licowax C, Clariant). Soil elemental analysis results are displayed in supplementary Table S2.

Table 1
Summary of P species detected in the soils from Hawaii with various spectroscopic techniques. Ca-P = calcium phosphate; Al-P = aluminum associated P; Fe-P = iron associated P. Soil P speciation generally shifts from apatite and adsorbed P at drier sites, to organic and adsorbed P at wetter sites.

	Site-Horizon		Rainfall (mm)	XRD	P K-edge bulk-XANES (SSRL, beamline 14–3)	P K-edge bulk-XANES (BESSY II, KMC-1)	P $L_{2,3}$-edge XANES (CLS, VLS-PGM)	P K-edge micro-XANES (Soleil, LUCIA) *[Number (X) is amount of spectra collected with this compound]*	P K-edge micro-XANES (ESRF, ID21) *[Number (X) is amount of spectra collected with this compound]*	micro-Raman (532 nm)
1		A	275	Apatite	adsorbed P	organic/adsorbed P, Ca-P	not detected	organic/adsorbed P (11), Ca-P (9)	not investigated	Apatite (high)
		B	275	Apatite	adsorbed P, Ca-P	organic/adsorbed P, Ca-P	not detected	not investigated	Ca-P (35), organic/adsorbed P (5)	Apatite (high)
2		A	316	Apatite	adsorbed P, Ca-P	organic/adsorbed P, Ca-P	not detected	organic/adsorbed P (18), Al-P (2)	Ca-P (31), organic/adsorbed P (27)	Apatite (high)
		B	316	Apatite	adsorbed P, Ca-P	organic/adsorbed P, Ca-P	not detected	not investigated	Ca-P (29), organic/adsorbed P (9)	Apatite (high)
3		A	1340	Crandallite	Al-P, adsorbed P	Al-P	Al-P	Al-P (15), Ca-P (1)	Al-P (41)	Apatite (low)
		B	1340	Crandallite	Al-P, adsorbed P	Al-P	not detected	not investigated	Al-P (37), Ca-P (3)	Apatite (low)
4		A	1578	Crandallite	adsorbed P	organic/adsorbed P	not detected	not investigated	not investigated	not detected
		B	1578	Crandallite	Al-P, adsorbed P	Al-P	Al-P	not investigated	Al-P (30), Ca-P (10)	not detected
5		A	2163	not detected	adsorbed P, Fe-P	organic/adsorbed P, Fe-P	Fe-P	organic/adsorbed P (18); Fe-P (2)	organic/adsorbed P (27), Ca-P (3)	not detected
		B	2163	not detected	adsorbed P	organic/adsorbed P	Fe-P	not investigated	organic/adsorbed P (34)	not detected
6		A	3123	not detected	organic/adsorbed P	organic/adsorbed P	not detected	organic/adsorbed P (16), Al-P(1), Ca-P (1)	organic/adsorbed P (45), Al-P (2), Ca-P (2)	Apatite (low)
		B	3123	not detected	adsorbed P	organic/adsorbed P	not detected	not investigated	organic/adsorbed P (53)	not detected

2.2. X-ray diffraction analysis

The mineralogy of the soils and parent material was characterized by powder X-ray diffraction (XRD). Samples were finely ground using a McCrone Micronizing Mill (McCrone Scientific Ltd, London, UK) and homogeneously packed into powder sample holders. The samples were analyzed on a Bruker D8 Advance diffractometer using Cu $K\alpha_{1,2}$ radiation and a high-resolution energy-dispersive 1D detector (Bruker AXS GmbH, Karlsruhe, Germany). The data were collected in Bragg-Brentano geometry from 4° to 70°2θ with 0.02°2θ steps and 10 s acquisition time per step. For the determination of "amorphous" matter contents, X-ray diffractograms were also collected after mixing powdered samples with 33% w/w crystalline corundum powder (Al_2O_3) as an internal standard. The diffractograms were analyzed with Rietveld quantitative-phase analysis using TOPAS Version 5 (Bruker DIFFRAC.SUITE). Because the X-ray "amorphous" fraction of the soils can contain both organic matter and amorphous or poorly-crystalline inorganic material, the concentration of organic matter, determined by measuring organic C and multiplying by a factor of two (Pribyl, 2010), was subtracted from the amorphous fraction to approximate the concentration of amorphous or poorly-crystalline inorganic matter.

2.3. Phosphorus K-edge bulk-XANES spectroscopy

Bulk Phosphorus *K*-edge XANES spectroscopic measurements of all soil samples were carried out at two different synchrotron facilities – Stanford Synchrotron Radiation Lightsource (SSRL) at SLAC National Accelerator Laboratory in California, United States and Berlin Electron Storage Ring Society for Synchrotron Radiation (BESSY II) at Helmholtz-Zentrum Berlin (HZB), Germany. At beamline 14–3 of the SSRL, incident beam energy was selected using a Si(1 1 1) double-crystal monochromator, and storage ring current was 495–500 mA in top-up mode. P *K*-edge XANES spectra were measured in fluorescence mode using a Vortex Si-drift solid-state detector (Canberra) in a helium atmosphere from 2130 eV to 2200 eV in steps of 0.2 eV at room temperature; sample preparation and data collection were conducted as described in Massey (2019). Monochromator energy calibration was achieved by setting the top of the *K*-edge peak of the lazulite XANES spectrum to 2153.5 eV

At BESSY II, measurements were conducted in the High Kinetic Energy Photoelectron Spectrometer (HIKE) endstation (Gorgoi et al., 2009) located at the KMC-1 beamline (Schaefers et al., 2007). The ring was operated in top-up mode with a beam current of 280 mA. Like at SSRL, this beamline also uses a Si (1 1 1) double-crystal monochromator. P *K*-edge XANES spectra were measured in fluorescence mode using a Si-drift detector, XFlash® 4010 (Bruker, Berlin, Germany) from 2130 eV to 2200 eV in steps of 0.25 eV at room temperature. Monochromator energy was calibrated against the first derivative maximum of β-tricalcium phosphate at 2152.0 eV.

Phosphorus *K*-edge XANES spectra were analyzed using the program *Athena*, part of the *Demeter* software package version 0.9.24 (Ravel and Newville, 2005). The E0 edge energy was chosen as the maximum of the first derivative of the data. Spectra were background-corrected using a linear regression fit through the pre-edge region (−18 to −8 eV relative to E_0) and a polynomial regression fit through the post-edge region (E_0 + 30 to +47 eV). The features of the P *K*-edge XANES spectra were compared qualitatively to reference spectra of various P compounds (Fig. S1a top and Fig. S2). The features at the following energies were used for identification and are marked in Fig. S1a: Ca-P – peaks at 2155.5 eV, 2163 eV and 2170 eV, Al-P – strong peak at 2171 eV, Fe-P – pre-edge peak at 2149.5 eV and organic/adsorbed P – none clear feature after the edge.

2.4. Phosphorus K-edge micro-XANES spectroscopy

Micro-XRF maps and micro-XANES spectra were collected from

nearly each soil sample (see Table 1) at: the ID21 X-ray microscopy beamline ((Cotte et al., 2017); beam size 0.7 × 1.2 μm^2) at the European Synchrotron Radiation Facility (ESRF); the LUCIA beamline ((Vantelon et al., 2016); beam size 5 × 5 μm^2) at the Synchrotron Soleil; and, at beamline 14–3 at SSRL (beam diameter ~2 μm). Monochromator energy was calibrated against the first derivative maximum of β-tricalcium phosphate at 2152.0 eV at ESRF and Soleil, respectively, and lazulite at 2153.5 eV at the SSRL. At ESRF and Soleil, measurements were performed at room temperature and under vacuum (10^{-2} mbar), while at SSRL measurements were conducted in a helium atmosphere. First, two-dimensional micro-XRF elemental maps (ranging from 106 × 112 μm^2 to 300 × 300 μm^2) were collected above the P *K*-edge by raster scanning the sample with respect to the X-ray beam with a step size of 0.7–5 μm, depending on beam geometry. Afterwards, finer micro-XRF maps were collected from interesting map regions. On selected points of interest, P *K*-edge micro-XANES spectra were collected from 2130 to 2200 eV with 0.2–2 eV energy steps. All measurements were performed by collecting the fluorescence signal, using a Si-drift detector. To optimize the discrimination of the various XRF line contributions, the XRF spectra from ESRF and Soleil were batch fitted at each map pixel using the PyMCA software (Solé et al. 2007). At the SSRL the software Sam Webb's SMAK (Sam's Microanalysis Toolkit; Webb, 2011) was used for fitting and image processing. The P *K*-edge XANES spectra were processed using the normalization and analysis procedures implemented in *Athena* (Ravel and Newville, 2005; see 2.3).

2.5. Micro-Raman spectroscopy

Micro-Raman spectroscopy analysis was performed on each soil sample using a Horiba LabRAM HR800 Raman microspectrometer equipped with a green 532 nm laser, 600 g/mm grating and a thermoelectrically cooled CCD operated at −60 °C. The spectrometer was calibrated using the 520.5 cm^{-1} band from a silicon wafer. Soils were pelleted to provide a flat sample surface and a 50× objective was used to focus the laser onto the sample. The power of the laser was ca. 3 mW at the sample surface, and the Raman scattered light was collected in a back-scatter geometry. Two independent maps of 150 × 120 μm^2 were acquired from each sample with 5 μm steps, and the samples were exposed to the laser for 10 s prior to spectral acquisition to decrease the effect of the high fluorescence background in soil. Typical acquisition times were 12 accumulations of 5 s integrations (for a total of 60 s per final spectrum), depending on the sample. The grating was fixed to center at 1050 cm^{-1} throughout spectrum acquisition. Random spikes due to cosmic rays were removed as part of the process of accumulating and combining multiple spectra.

The acquired data (spectra and maps) were processed using the LabSpec 6 software. All spectra were pre-processed by truncating to 1800–250 cm^{-1}, de-noising and by baseline correction by a 7° polynomial function, before being normalized to the broad background fluorescence intensity between 1350 and 1000 cm^{-1}. Regions with significant Raman features above the fluorescent background were identified by screening each pixel; extracted spectra were compared to reference spectra on the RRuff database (Lafuente et al., 2016) to identify the mineral. Maps were generated by integrating the area under the most intense peak identified for each mineral.

2.6. Backward trajectories of dust particles

The LAGRANTO Lagrangian analysis tool (Sprenger and Wernli, 2015) was used to calculate air parcel trajectories, using horizontal and vertical wind data from forecast models. The tool used meteorological data from ERA-Interim (Dee et al., 2011), produced by the European Centre for Medium-Range Weather Forecasts (ECMWF).

Trajectories of 4 μm dust particles were calculated by adding the sedimentation of dust particles to the vertical movement of air in the calculation of air parcel and dust trajectories. Four μm was chosen for dust deposition modeling because it is representative of both commonly-deposited dust particles on Hawaii, and of the smaller dust particles observed in this study (Jackson et al., 1971). The terminal sedimentation velocity was calculated using Stokes' equation. Backwards dust particle trajectories were calculated using a 14-day timeframe, starting close to the Kohala sampling location (20°N, 155°W) and 8 nearby locations (± 0.5° in latitude and longitude) every 6 h starting from 1 January 2007 to 31 December 2017 at 5 pressure levels (500, 600, 700, 800, 900 hPa). Trajectories originating from potential desert areas were then identified. The liquid water content of the ERA-Interim data was also used to distinguish whether the air parcel encountered clouds and precipitation, which could scrub the mineral aerosols from the air parcel.

3. Results

3.1. Soil mineralogy and P minerals

According to the XRD analyses, soil from arid sites still contained primary minerals (e.g., plagioclases, apatite) likely derived from the abundant coarse fragments in these shallow, skeletal soils. By contrast, soils from humid sites were composed entirely of “amorphous” or poorly-crystalline secondary-minerals like oxides, organic matter, and dust-derived minerals such as quartz. Differences in soil mineralogy between sites and horizons within the same domain were small compared to differences between soil samples from different domains (Fig. 1), as predicted by Vitousek and Chadwick (2013). Parent material samples were composed primarily of plagioclases, alkali feldspars, and pyroxenes with 56 g kg^{-1} apatite (Table S3). Parent material samples contained no quartz. On arid sites (1 and 2), amorphous minerals were the dominant fraction, though primary minerals were present in smaller concentrations. On the subhumid sites (3 and 4), remaining primary mineral concentrations were even lower, or primary minerals disappeared completely, while soil organic matter concentrations increased (> 100 g organic matter kg^{-1}). Soils at subhumid sites were enriched in phosphates, but the dominant crystalline phosphate mineral according to XRD was crandallite ($CaAl_3(PO_4)_2(OH)_5{\cdot}H_2O$), rather than apatite (Table S3). On the humid sites (5 and 6), soil organic matter and amorphous or poorly-crystalline minerals dominated. On these sites, no crystalline P minerals were detectable by XRD. Quartz concentrations increased continuously along the rainfall gradient from 12 g kg^{-1} in the A horizon of the most arid site (site 1), to 92 g kg^{-1} in the A horizon of the most humid site (site 6, Table S3), with a similar pattern in the B horizon.

Fig. S1a shows the P *K*-edge bulk-XANES spectra of the Hawaiian soils (A and B horizon). In comparison to P reference spectra (Fig. S2), Ca-P was detected in the soils from arid sites (1A, 1B, 2A and 2B) by bulk P *K*-edge XANES spectroscopy. Since we saw a clear apatite signal with XRD, the Ca-P in sites 1A, 1B, 2A, and 2B is likely to be largely associated with apatite. Furthermore, the characteristic form of the XANES spectra of 3A, 3B, 4B shows aluminum-associated phosphate species (Giguet-Covex et al., 2013). The humid sites (5, 6) show mainly organic and/or adsorbed P. Furthermore, a pre-edge feature of iron-associated P (Fe-P) was detected in the P *K*-edge XANES spectrum of 5A. However, Fe-P in soil tends to be underestimated by P *K*-edge XANES (Prietzel and Klysubun, 2018). P $L_{2,3}$-edge XANES spectroscopy was also applied, but distinct spectral features were not readily apparent (Fig. S2b, methods and results in SI). In comparison to P $L_{2,3}$-edge XANES reference spectra (Fig. S3), spectra from sites 3A and 4B may indicate an Al-P, while spectra from 5A and 5B may indicate P adsorbed to Fe compounds (Xiong et al., 2012).

3.2. Micro-XRF mapping and P K-edge micro-XANES spectroscopy

Micro-XRF mapping revealed that Al associated P was relatively homogeneously distributed at the micro-scale, whereas Ca-P was

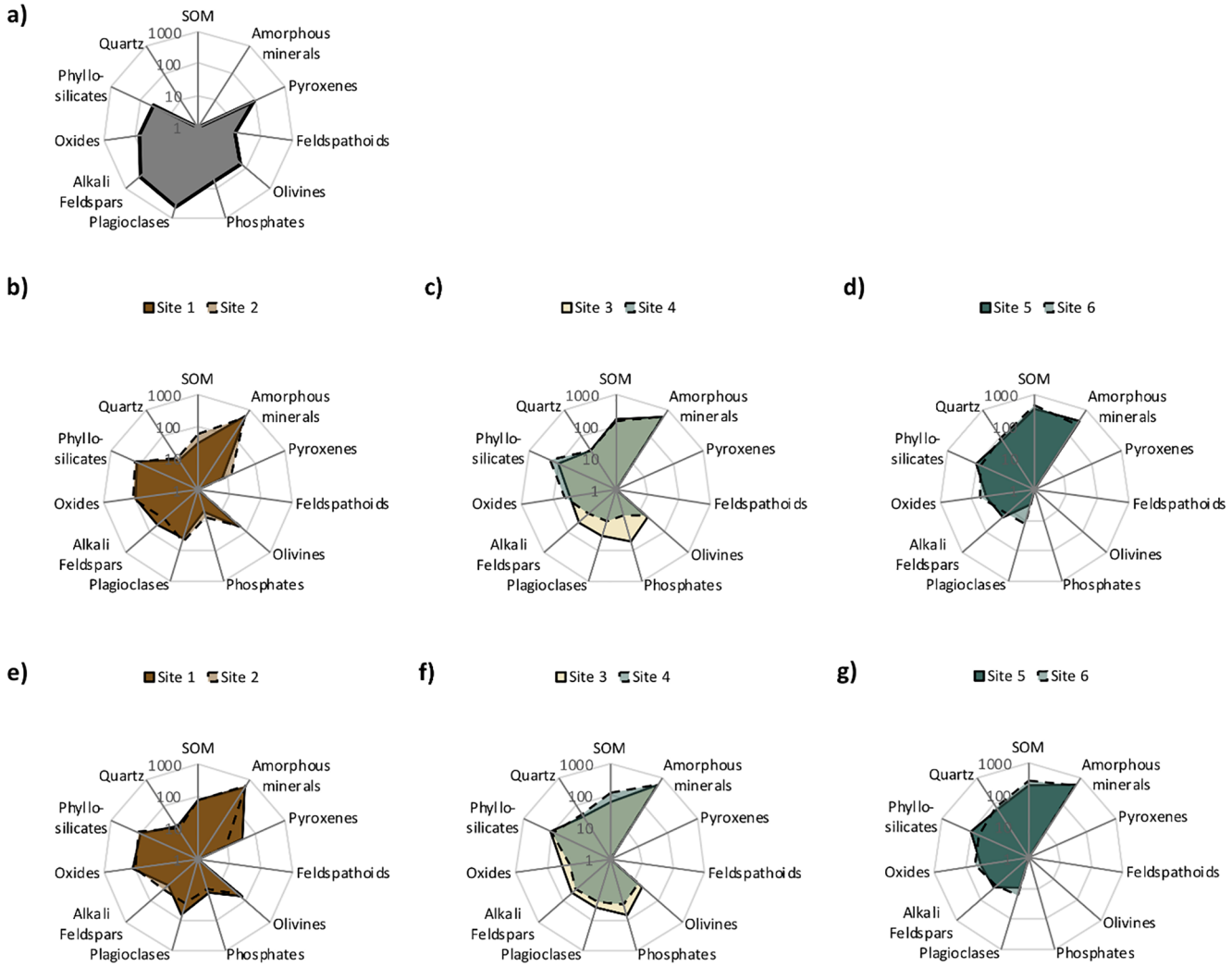


Fig. 1. Minerals in the parent material (a), A horizon soil samples (b-d), and B horizon soil samples (e-g), as determined by XRD. In the parent material (a), and the A and B horizon of soils in sites 1 and 2 (b, e), the dominant phosphate mineral was apatite. In the A and B horizon of soils in sites 3 and 4 (c and f) the dominant phosphate mineral was crandallite. See also supplementary Table S3. Scale in g kg^{-1}.

located in P "hotspots," areas with significantly higher P concentration (all results in Table 1). In sites 1 and 2, where apatite was a dominant P form, the P hotspots spatially co-occurred with Ca hotspots. In the remaining sites, P was more homogeneously distributed, with only a few P hotspots. However, smaller isolated P hotspots were also found in surface soils (A horizon) from the most humid sites 5 and 6, and these also co-occurred with Ca (Fig. 2b and S4). The Ca and P hotspots in sites 5 and 6 had diameters ranging between 5 and 30 μm. However, no similar P hotspots were found in subsurface (B horizon) soil samples from sites 5 and 6.

P *K*-edge micro-XANES spectra obtained in combination with the micro-XRF maps revealed that spectra from low P-concentration areas in all samples were characteristic of Al-associated P or organic/adsorbed P, while spectra from the hotspots had characteristic Ca-P features (Fig. 2). The micro-XANES spectra thus explained the spatial co-occurrence of Ca and P at the micro-scale observed via micro-XRF mapping. Ca-P features were also observed in the above-described P hotspots in sites 5 and 6, where all primary minerals have weathered away, and no apatite was expected (Figs. S4–S6). While in drier sites 1–4, Ca-P spots were more common in the B horizon, in site 5 and 6 Ca-P spectra were only found in the A horizon (Table 1). On its own, XANES spectroscopy did not allow differentiation between apatite and other Ca-P forms due to similarities between features in Ca-P reference spectra (Fig. S2).

3.3. Micro-Raman spectroscopy

Micro-Raman spectroscopy identified apatite in the arid sites 1 and 2 (see Fig. 3 bottom left, and Table 1), corroborating the XRD and XANES analyses. The observed Raman peak at 965 cm^{-1} overlapped with that of apatite reference spectra from the RRUFF database (Supplementary Fig. S7). In these sites, micro-Raman spectra also indicated forsterite and anatase, but no quartz. At the most humid site, in the surface horizon (site 6A), on the other hand, micro-Raman spectroscopy revealed an abundance of quartz crystals, corroborating the XRD results and indicative of the expected dust deposition gradient. A Raman band of apatite was also detected at site 6A, though the apatite signal was much weaker than in arid sites (Fig. 3, bottom right). The detection of apatite at site 6A complemented the micro-XANES analyses, which had found Ca-P, but were not conclusive regarding the type of Ca-P mineral.

3.4. Dust backward trajectories

To explore the origin of continental dust delivered to Hawaii, dust particle (r = 4 μm) backward trajectories were calculated (Fig. 4). Because the maximum height of dust during sand storms in the source regions is 5 – 6 km (Tsamalis et al., 2013), only trajectories which originated from dust source regions and from pressure levels > 500 hPa (height below 5500 m) were shown in Fig. 4. In addition, trajectories

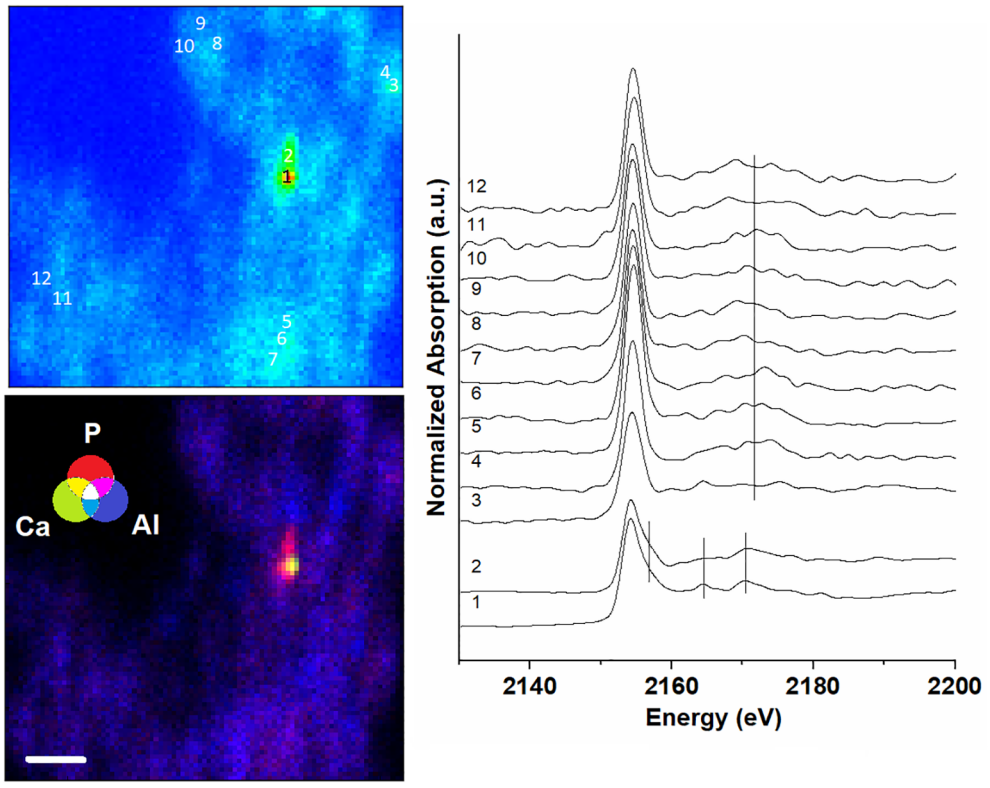


Fig. 2. XRF map of P, Ca and Al (left bottom; 0.7 μm step; color scale is arbitrary; white bar is 10 μm), P map with selected points of interest for micro-XANES (left top; red = high concentration, blue = low concentration), and micro-XANES spectra (right, vertical lines show features of same compound) of the soil sample 6A, analyzed at ID21 beamline, ESRF. The Ca-P grain shown on the map is approximately 5 × 10 μm^2. (For interpretation of the references to color in this figure legend, the reader is referred to the web version of this article.)

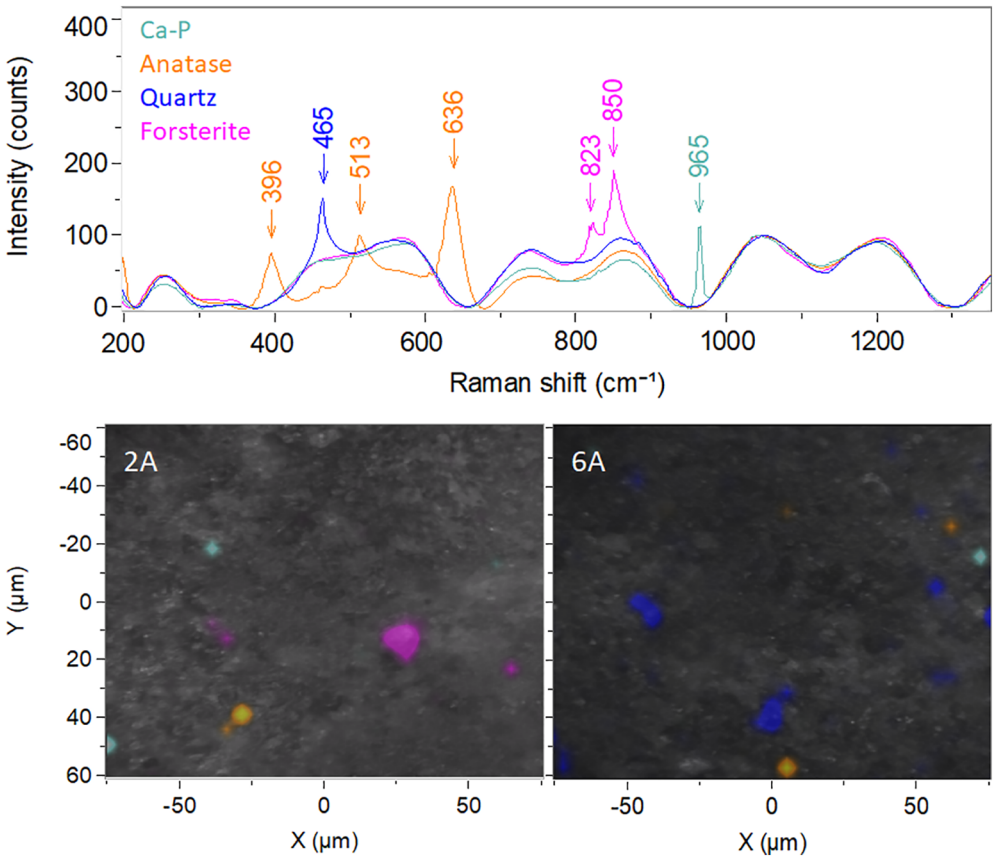


Fig. 3. Raman images (bottom) and corresponding spectra of compounds (top) from the soils 2A and 6A. Apatite and anatase particles were observed in both soils, while forsterite was observed in soil from site 2A, and quartz was observed in soil from site 6A.

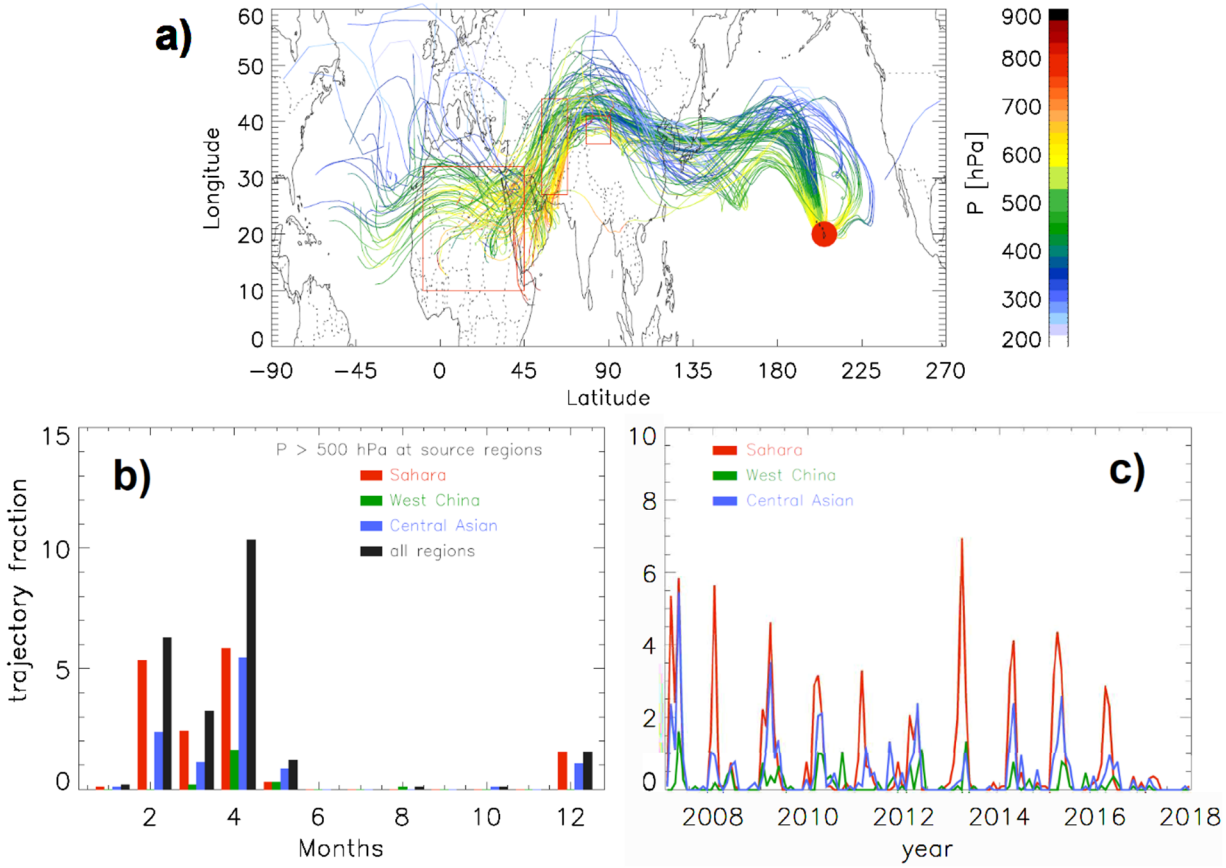


Fig. 4. a) Backwards trajectories of dust particles with radius of 4 μm, starting from Hawaii at 700 hPa (approx. 3000 m) level. Only trajectories were shown, which originated from the desert regions (marked by the red boxes) with P > 500 hPa (below 5500 m) and did not encounter liquid clouds (liquid water content < 50 ppm) before reaching Hawaii; b) The fraction of particle trajectories of r = 4 μm originated from deserts regions with P > 500 hPa and did not encounter liquid clouds for the year 2007; For reference, the fraction of all trajectories which originated from deserts regions with P > 500 hPa were also shown by the unfilled bars; c) The fraction of particle (r = 4 μm) trajectories which originated from deserts regions and did not encounter liquid clouds before reaching Hawaii at 700 hPa level of the years 2007–2017. (For interpretation of the references to color in this figure legend, the reader is referred to the web version of this article.)

which encountered liquid clouds with a liquid water content > 50 mg kg^{-1} were excluded. Calculated trajectories showed that dust from known dust source areas in Central Asia and Northern Africa regularly reaches the Hawaiian archipelago (Fig. 4a). The calculations show dust particles that start at a height below 5500 m (pressure > 500 hPa) in the selected dust regions (red boxes) and end at approximately 3000 m height (700 hPa) above Hawaii may be delivered from the atmosphere to the Kohala peninsula by rain (see Porder et al., 2007 for more information regarding the dust rain-out effect on Kohala). The fraction of trajectories arriving in Hawaii from dust sources in the Sahara, Western China, and Central Asia is highest in Northern Hemisphere winter/spring (December-May) of each year. In April, over 10% of air mass trajectories arriving in Hawaii stem from these dust source centers and meet the requirements for dust transport (Fig. 4b). Furthermore, though farthest away (but biggest by area), dust trajectories originating from the Sahara are more common than from Asian dust centers. These patterns were relatively stable for the ten-year calculation period (2008–2017) (Fig. 4c).

4. Discussion

A broad ensemble of non-invasive spectroscopic techniques was used to measure P speciation along a climatic gradient on Hawaii, providing insights on the impact of dust deposition on soil P speciation. In particular, micro-Raman spectroscopy, which has rarely been used to study P species in soil, here allowed more robust conclusions about dust-derived, collocated quartz and apatite P in Kohala soils (Table 1). In general, we observed the expected change from apatite to organic P and adsorbed inorganic P, and some secondary Al-P and Fe-P minerals with increasing rainfall (Helfenstein et al., 2018; Prietzel et al., 2013). Micro-spectroscopic methods also revealed apatite in surface soils of the most humid sites (soil 5A: Fig. S4; soil 6A: Figs. 2,3, S5, S6), which are devoid of minerals from parent material; quartz and apatite in these soils are therefore likely to be deposited as dust. However, while quartz, which is absent in Hawaiian basalt, is a well-known indicator of transcontinental dust transport, apatite grains could result both from local or transcontinental dust sources.

While trends in apatite in sites 1–4 can be explained by the gradual weathering of parent material (Chadwick et al., 2003; Ziegler et al., 2003), the small apatite grains found in surface soils of the most humid sites 5 and 6 represent an altogether different process, with an altogether different source. Because of the high amount of rainfall at these locations, remnants of apatite from the parent material are very unlikely in the topsoil. X-ray diffraction analyses of the soil mineralogy indicated that in soils at the most humid sites, amorphous or poorly-crystalline secondary minerals and dust-derived minerals are dominant, rather than primary minerals (Fig. 1 and Table S3). The low soil pH of these humid sites (pH < 5.5) and the low Ca and P concentrations preclude re-precipitation of apatite-like minerals (Vitousek and Chadwick, 2013). Furthermore, apatite was only found in the surface soil (A horizon), but not the subsurface (B horizon) of these soils. By analyzing peat layers in a German bog, it was shown that calcite and apatite could only be identified in the top layers, which are youngest, while quartz was found at all depths because it is much more resistant

to weathering (Le Roux et al., 2006). Thus, it might be possible that quartz in our samples remains in the B horizon while apatite does not remain in subsoil horizons because it dissolves readily. However, bioturbation of the soils by soil fauna (e.g. worms) is also possible, resulting in mixing of the surface and subsurface soil. It is possible that apatite grains were also present in the B horizon, but highly dispersed and therefore not captured by the area of soil mapped in our experiment (Adediran et al., 2020).

One possible origin of aeolian apatite inputs might be the nearby active volcanos. The Kilauea volcano on the island of Hawaii (approx. 100 km from the study sites on the Kohala peninsula) has been active since 1983, erupting almost continuously since that time. The eruption of the Kilauea volcano is effusive rather than explosive, leading to a steady lava flow out of the volcano, without the production of much dust. However, small explosions may send magma particles into the atmosphere, including long strings of supercooled Hawaiian basalt lava (called Pele's hair), which may travel considerable distances by wind due to their high surface area (Katsura, 1967). Additionally, the aerosol plume from the Kilauea volcano contains several pollutants and nutrients (including apatite), with deposition rates > 50 times higher than background rates (MacDonald, 1949; Sansone et al., 2002). However, like the parent material at the Kohala study site, material from the active volcano is basaltic and does not contain quartz. Although the apatite particles observed in this study could come from the Kilauea volcano, the prevailing winds carry most of the tephra and gases in a southerly direction, away from Kohala.

Alternatively, the observed apatite grains may be blown over from sugar cane growing areas on the northeastern Hawaii coast, where various kinds of phosphates were applied as fertilizer. However, the sugar cane industry has all but disappeared from the island since the 1980s (Melrose et al., 2015).

Meanwhile, there is abundant evidence that intercontinental tropospheric dust transport can deliver quartz and other minerals to Kohala. Many researchers have documented continental dust fall in the North Pacific from shipboard measurements (Betzer et al., 1988) and deep-sea cores (Blank et al., 1985; Nakai et al., 1993; Rea, 1994). Deep-sea cores show that the mass accumulation rate of dust decreases from 1000 mg cm^2 kyr^{-1} near the Japanese coast to < 50 mg cm^2 kyr^{-1} around Hawaii (Rea, 1994). Considerable amounts of dust still make it to the Hawaiian Islands, as has been shown by soil and isotopic analyses (Chadwick et al., 1999; Jackson et al., 1971; Rex et al., 1969). Tropospheric transport of dust to Hawaii is indicated by the backward trajectories of dust particles calculated in this study. While earlier work assumed that dust arrives from central Asia (Chadwick et al., 1999; Merrill et al., 1989; Pye and Zhou, 1989), the dust trajectories reported herein suggest that dust on Hawaii may also be sourced from the Sahara, the Middle East, or other Northern hemisphere locations.

Over 10% of air masses arriving in Hawaii in April originate from a height below 5500 m in the dust source areas of the Sahara, central Asia, or Western China (Fig. 4). In order for dust to reach Hawaii, it must reach a height of 5500 m in the starting region; dust can only reach these heights during sandstorms. Sandstorms in the Sahara Desert and Asian deserts are mostly between April and September and March to May, respectively (Wiacek et al., 2010). Thus, there is an overlap between favorable conditions for tropospheric dust generation and transport to Hawaii in March through May.

While large particles fall out faster and are thus less likely to be transported across the Pacific, even the largest apatite dust particles observed here (~30 μm) could originate from tropospheric transport. The observed apatite dust particles ranged in diameter between 5 and 30 μm. Other investigators have estimated that around 70% of dust-derived quartz in Hawaiian soils is in the range of 2–10 μm in diameter (Jackson et al., 1971). However, the transport of considerably larger dust particles (> 75 μm) from the continents to the North Pacific is also well-documented (Betzer et al., 1988; van der Does et al., 2018). Hence even the largest apatite-like particle observed in this work, with a diameter of ~30 μm, is within the range of those that may have originated from tropospheric transport, though the mechanisms of tropospheric transport of such large particles are still unclear (van der Does et al., 2018), and could thus not be modeled via the backward trajectory approach used herein.

Globally, dust loading tends to occur in dry areas such as the deserts of Central Asia or the Sahara (Okin et al., 2004; Rea, 1994). In these dry areas, soil pH tends to be high (Slessarev et al., 2016), and P is mostly in the form of apatite (Yang et al., 2013). As a consequence, P in dust from these regions is also mostly in the form of apatite (Bristow et al., 2010; Gross et al., 2016; Gu et al., 2019; Lu et al., 2006; Stockdale et al., 2016; Swap et al., 1992). It is therefore likely that apatite particles in the humid sites of the Kohala peninsula are signs of intercontinental dust transport. While micro-XANES and micro-Raman spectroscopy cannot provide quantitative information on soil P forms, apatite is unlikely to account for more than a few percent of total P in these soils, otherwise apatite-like spectral features would be apparent in the bulk P *K*-edge XANES spectra. A rough estimate of the amount of dust-derived apatite present in these soils can be made by estimating annual P dust input, combined with an estimate of the rate of apatite dissolution.

Using rare earth elements, long-term (over millennia) aerosol P fluxes to Kohala have been approximated at around 0.9 mg P m^{-2} yr^{-1} (Chadwick et al., 1999; Kurtz et al., 2001; Porder et al., 2007). However, in recent decades, global atmospheric P loading has been much higher due to combustion of fossil fuels, mining, agriculture, and land use change (Wang et al., 2015). Recently, atmospheric P deposition measured with dust traps averaged 30 mg P m^{-2} yr^{-1} in Oceania (Tipping et al., 2014). About 90% of P in dust is apatite (Stockdale et al., 2016), giving an annual input of 27 mg P m^{-2} yr^{-1} as apatite. Apatite dissolution is dependent on temperature, pH, solution saturation state, apatite composition, and apatite surface area (Guidry and Mackenzie, 2003). While temperature and pH are known for Kohala soils, solution saturation state, apatite composition, and its surface area are not, and likely very different in the *in situ* soil environment, as compared to laboratory conditions. Also, the abundance of organic acids may inhibit dissolution, leading to much slower apatite dissolution in organic matter-rich soils (Le Roux et al., 2006). Due to these uncertainties, the rate of apatite dissolution for dust-derived apatite grains in Kohala soils cannot be determined theoretically, but should be based on observational data. In a peat bog in Germany, dust-derived apatite was found to persist to a depth of 8 cm, which ^{210}Pb and ^{14}C based age-depth modeling showed to be 50–100 years old (Le Roux et al., 2006). Similarly, by studying dust inputs along a chronosequence, it was estimated that dust-derived apatite grains endured up to 200 years in wet, low pH soils in New Zealand (Eger et al., 2013), under cooler temperatures than on the island of Hawaii. The persistence of apatite reported in these previous studies is instructive regarding the dissolution of dust-derived apatite in humid, acidic soils, but previous studies did not report detection limits of apatite, so it is not clear what fraction of apatite remaining ($P(t)/P_0$) corresponds with the reported timeframes. Assuming a first-order decrease of apatite, and considering possible combinations of the reported persistence times, and considering reasonable values for fractions of apatite remaining to fall below detection limits (0.01, 0.1, and 0.2), we can approximate a range of apatite dissolution rates with a simple, explorative model (see SI for details).

Given the annual apatite input as dust (up to 27 mg m^{-2} yr^{-1}), and a range of potential apatite dissolution rates (0.008–0.092 mg m^{-2} yr^{-1}), dust-derived apatite stocks are likely on the order of 10 – 100 mg P kg^{-1} soil for the most humid Kohala site, site 6 (see SI for details). The upper estimates of the amount of dust-derived apatite are similar to the HCl-extractable P pool in sequential extractions for the wettest site (125 mg P kg^{-1}, according to Helfenstein et al., 2018). However, while the HCl-P pool is often considered to extract P from apatite, in these soils the HCl-P pool also contains secondary P minerals (Helfenstein et al., 2018). Sequential

extraction by itself is therefore not a robust indicator for apatite (Gu et al., 2020; Helfenstein et al., 2020; Tamburini et al., 2012), be it from parent material or dust-derived sources. For example, the HCl-P pool is larger in the B horizon of site 6 (847 mg P kg^{-1}), than in the A horizon (125 mg P kg^{-1}). However, here it is likely fully composed of secondary P minerals, as we found no apatite grains in the B soil horizon.

5. Conclusion

Apatite is generally perceived to occur as a remnant of parent material in relatively unweathered soils. However, in the present study, analysis of P speciation along a rainfall and dust-deposition gradient revealed the presence of dust-derived apatite grains in the highly weathered soils from a humid climatic regime. Dust-derived apatite was observed by micro-XRF mapping coupled with P *K*-edge micro-XANES spectroscopy, as well as micro-Raman spectroscopic analysis. Furthermore, apatite grains were found in a soil layer also containing quartz grains, another indicator of continental dust. Though it was not possible to pinpoint the origin of individual apatite grains, and some may also be of local origin (e.g. from volcanoes), theoretical calculations based on annual apatite input via dust and apatite dissolution suggest that dust-derived apatite may constitute 10–100 mg P kg^{-1} soil in surface soil horizons.

The analyses reported in this work add further evidence that dust P inputs, which are largely as apatite, may take decades to dissolve even under acidic soil conditions in a humid climate. Additionally, the presence of dust-derived apatite in relatively isolated Hawaiian soils suggests that dust-derived apatite may also be present in other highly-weathered soils, previously thought to be apatite-free. While aeolian apatite inputs are comparatively negligible for younger soils very rich in P, for low-P soils such as those found in most lowland tropical rainforests, dust-derived P inputs of a similar magnitude would be an important component of P dynamics, helping to support ecological productivity. And since Hawaii is not a very dusty place by global standards, one might expect other soils, closer to dust source areas, to have larger dust-derived apatite inputs. The application of micro-spectroscopic techniques, especially a combination of micro-XANES and micro-Raman spectroscopy, was instrumental here in identifying dust-derived quartz and apatite minerals, and similar techniques could be applied in other highly-weathered soils. With further evidence of dust-derived apatite grains, it may be necessary to reconsider our understanding of the presence and role of apatite in highly-weathered soils.

Declaration of Competing Interest

The authors declare that they have no known competing financial interests or personal relationships that could have appeared to influence the work reported in this paper.

Acknowledgments

The CLIMP project (Forms and dynamics of soil phosphorus along a climosequence on basalt-derived soils) was funded by the Swiss National Science Foundation (Project number 200021_162422). CV thanks the German Research Foundation (VO 1794/4-1) for financial support. Synchrotron analyses were conducted on the LUCIA beamline at Synchrotron Soleil (proposal 20160117), KMC-1 beamline at Helmholtz-Zentrum Berlin (BESSY II), ID21 beamline at the European Synchrotron Radiation Facility, beamline 14-3 at Stanford Synchrotron Radiation Source, and the VLS-PGM beamline at the Canadian Light Source. We thank these institutions for allocation of beamtime. The Stanford Synchrotron Radiation Lightsource, SLAC National Accelerator Laboratory, is supported by the U.S. Department of Energy, Office of Science, and Office of Basic Energy Sciences under Contract No. DE-AC02-76SF00515. The Canadian Light Source is supported by the Canada Foundation for Innovation, Natural Sciences and Engineering Research Council of Canada, the University of Saskatchewan, the Government of Saskatchewan, Western Economic Diversification Canada, the National Research Council Canada, and the Canadian Institutes of Health Research. The authors would like to express our thanks to the many scientists and staff of these exceptional research facilities, whose dedication and steadfast support made our work possible.

Appendix A. Supplementary data

Supplementary data to this article can be found online at https://doi.org/10.1016/j.geoderma.2020.114681.

References

Adediran, G.A., Tuyishime, J.R.M., Vantelon, D., Klysubun, W., Gustafsson, J.P., 2020. Phosphorus in 2D: spatially resolved P speciation in two Swedish forest soils as influenced by apatite weathering and podzolization. Geoderma 376, 114550. https://doi.org/10.1016/j.geoderma.2020.114550.

Betzer, P.R., Carder, K.L., Duce, R.A., Merrill, J.T., Tindale, N.W., Uematsu, M., Costello, D.K., Young, R.W., Feely, R.A., Breland, J.A., Bernstein, R.E., Greco, A.M., 1988. Long–range transport of giant mineral aerosol particles. Nature 336, 568–571. https://doi.org/10.1038/336568a0.

Blank, M., Leinen, M., Prospero, J.M., 1985. Major Asian aeolian inputs indicated by the mineralogy of aerosols and sediments in the western North Pacific. Nature 314, 84–86. https://doi.org/10.1038/314084a0.

Bristow, C.S., Hudson-Edwards, K.A., Chappell, A., 2010. Fertilizing the Amazon and equatorial Atlantic with West African dust. Geophys. Res. Lett. 37. https://doi.org/10.1029/2010GL043486.

Chadwick, O.A., Derry, L.A., Vitousek, P.M., Huebert, B.J., Hedin, L.O., 1999. Changing sources of nutrients during four million years of ecosystem development. Nature 397, 491–497. https://doi.org/10.1038/17276.

Chadwick, O.A., Gavenda, R.T., Kelly, E.F., Ziegler, K., Olson, C.G., Crawford Elliott, W., Hendricks, D.M., 2003. The impact of climate on the biogeochemical functioning of volcanic soils. Chem. Geol. 202, 195–223. https://doi.org/10.1016/j.chemgeo.2002.09.001.

Cotte, M., Pouyet, E., Salomé, M., Rivard, C., De Nolf, W., Castillo-Michel, H., Fabris, T., Monico, L., Janssens, K., Wang, T., Sciau, P., Verger, L., Cormier, L., Dargaud, O., Brun, E., Bugnazet, D., Fayard, B., Hesse, B., Pradas del Real, A.E., Veronesi, G., Langlois, J., Balcar, N., Vandenberghe, Y., Solé, V.A., Kieffer, J., Barrett, R., Cohen, C., Cornu, C., Baker, R., Gagliardini, E., Papillon, E., Susini, J., 2017. The ID21 X-ray and infrared microscopy beamline at the ESRF: status and recent applications to artistic materials. J. Anal. At. Spectrom. 32, 477–493. https://doi.org/10.1039/C6JA00356G.

Dee, D.P., Uppala, S.M., Simmons, A.J., Berrisford, P., Poli, P., Kobayashi, S., Andrae, U., Balmaseda, M.A., Balsamo, G., Bauer, P., Bechtold, P., Beljaars, A.C.M., van de Berg, L., Bidlot, J., Bormann, N., Delsol, C., Dragani, R., Fuentes, M., Geer, A.J., Haimberger, L., Healy, S.B., Hersbach, H., Hólm, E.V., Isaksen, L., Kållberg, P., Köhler, M., Matricardi, M., McNally, A.P., Monge-Sanz, B.M., Morcrette, J.-J., Park, B.-K., Peubey, C., de Rosnay, P., Tavolato, C., Thépaut, J.-N., Vitart, F., 2011. The ERA-Interim reanalysis: configuration and performance of the data assimilation system. Q. J. R. Meteorol. Soc. 137, 553–597. https://doi.org/10.1002/qj.828.

Doolette, A.L., Smernik, R.J., 2011. Soil organic phosphorus speciation using spectroscopic techniques. In: Bünemann, E.K. (Ed.), Phosphorus in Action. Springer, Heidelberg, pp. 3–36. https://doi.org/10.1007/978-3-642-15271-9.

Eger, A., Almond, P.C., Condron, L.M., 2013. Phosphorus fertilization by active dust deposition in a super-humid, temperate environment – soil phosphorus fractionation and accession processes. Global Biogeochem. Cycles 27, 108–118. https://doi.org/10.1002/gbc.20019.

Eriksson, A.K., Hillier, S., Hesterberg, D., Klysubun, W., Ulén, B., Gustafsson, J.P., 2016. Evolution of phosphorus speciation with depth in an agricultural soil profile. Geoderma 280, 29–37. https://doi.org/10.1016/j.geoderma.2016.06.004.

FAL, RAC, FAW, 1996. pH-Wert in Wassersuspension (1:2.5) & pH-Wert in CaCl2-Suspension (1:2.5). In: Schweizerische Referenzmethoden Der Eidgenössischen Landwirtschaftlichen Forschungsanstalten. Forschungsanstalt für Agrarökologie und Landbau (FAL), Recherche Agronomique Changins (RAC), Forschungsanstalt Wädenswil (FAW), Agroscope Zürich, Changins, Wädenswil.

Giambelluca, T.W., Chen, Q., Frazier, A.G., Price, J.P., Chen, Y.-L., Chu, P.-S., Eischeid, J.K., Delparte, D.M., 2013. Online rainfall atlas of Hawai'i. Bull. Am. Meteorol. Soc. 94, 313–316. https://doi.org/10.1175/BAMS-D-11-00228.1.

Giguet-Covex, C., Poulenard, J., Chalmin, E., Arnaud, F., Rivard, C., Jenny, J.P., Dorioz, J.M., 2013. XANES spectroscopy as a tool to trace phosphorus transformation during soil genesis and mountain ecosystem development from lake sediments. Geochim. Cosmochim. Acta 118, 129–147. https://doi.org/10.1016/j.gca.2013.04.017.

Gorgoi, M., Svensson, S., Schäfers, F., Öhrwall, G., Mertin, M., Bressler, P., Karis, O., Siegbahn, H., Sandell, A., Rensmo, H., Doherty, W., Jung, C., Braun, W., Eberhardt, W., 2009. The high kinetic energy photoelectron spectroscopy facility at BESSY progress and first results. Nucl. Instrum. Methods Phys. Res. Sect. A Accel. Spectrometers Detect. Assoc. Equip. 601, 48–53. https://doi.org/10.1016/j.nima.2008.12.244.

Gross, A., Turner, B.L., Goren, T., Berry, A., Angert, A., 2016. Tracing the sources of atmospheric phosphorus deposition to a tropical rain forest in panama using stable oxygen isotopes. Sci. Technol. Environ. https://doi.org/10.1021/acs.est.5b04936.
Gu, C., Hart, S.C., Turner, B.L., Hu, Y., Meng, Y., Zhu, M., 2019. Aeolian dust deposition and the perturbation of phosphorus transformations during long-term ecosystem development in a cool, semi-arid environment. Geochim. Cosmochim. Acta 246, 498–514. https://doi.org/10.1016/j.gca.2018.12.017.
Gu, C., Dam, T., Hart, S.C., Turner, B.L., Chadwick, O.A., Berhe, A.A., Hu, Y., Zhu, M., 2020. Quantifying uncertainties in sequential chemical extraction of soil phosphorus using XANES spectroscopy. Environ. Sci. Technol. 54, 2257–2267. https://doi.org/10.1021/acs.est.9b05278.
Guidry, M.W., Mackenzie, F.T., 2003. Experimental study of igneous and sedimentary apatite dissolution: control of pH, distance from equilibrium, and temperature on dissolution rates. Geochim. Cosmochim. Acta 67, 2949–2963. https://doi.org/10.1016/S0016-7037(03)00265-5.
Helfenstein, J., Tamburini, F., von Sperber, C., Massey, M.S., Pistocchi, C., Chadwick, O.A., Vitousek, P.M., Kretzschmar, R., Frossard, E., 2018. Combining spectroscopic and isotopic techniques gives a dynamic view of phosphorus cycling in soil. Nat. Commun. 9, 3226. https://doi.org/10.1038/s41467-018-05731-2.
Helfenstein, J., Pistocchi, C., Oberson, A., Tamburini, F., Goll, D.S., Frossard, E., 2020. Estimates of mean residence times of phosphorus in commonly-considered inorganic soil phosphorus pools. Biogeosciences 17, 441–454. https://doi.org/10.5194/bg-2019-192.
Hesterberg, D., 2010. Macroscale chemical properties and X-ray absorption spectroscopy of soil phosphorus. Dev. Soil Sci. 34, 313–356. https://doi.org/10.1016/s0166-2481(10)34011-6.
Hesterberg, D., McNulty, I., Thieme, J., 2017. Speciation of soil phosphorus assessed by XANES spectroscopy at different spatial scales. J. Environ. Qual. 46, 1190–1197. https://doi.org/10.2134/jeq2016.11.0431.
Jackson, M.L., Levelt, T.W.M., Syers, J.K., Rex, R.W., Clayton, R.N., Sherman, G.D., Uehara, G., 1971. Geomorphological relationships of tropospherically derived Quartz in the soils of the Hawaiian Islands1. Soil Sci. Soc. Am. J. 35, 515–525. https://doi.org/10.2136/sssaj1971.03615995003500040015x.
Katsura, T., 1967. Pele's hair as a liquid of Hawaiian tholeiitic basalts. Geochem. J. 1, 157–168. https://doi.org/10.2343/geochemj.1.157.
Kizewski, F., Liu, Y.-T., Morris, A., Hesterberg, D., 2011. Spectroscopic approaches for phosphorus speciation in soils and other environmental systems. J. Environ. Qual. 40, 751. https://doi.org/10.2134/jeq2010.0169.
Kruse, J., Abraham, M., Amelung, W., Baum, C., Bol, R., Kühn, O., Lewandowski, H., Niederberger, J., Oelmann, Y., Rüger, C., Santner, J., Siebers, M., Siebers, N., Spohn, M., Vestergren, J., Vogts, A., Leinweber, P., 2015. Innovative methods in soil phosphorus research: a review. J. Plant Nutr. Soil Sci. 178, 43–88. https://doi.org/10.1002/jpln.201400327.
Kurtz, A.C., Derry, L.A., Chadwick, O.A., 2001. Accretion of Asian dust to Hawaiian soils: isotopic, elemental, and mineral mass balances. Geochim. Cosmochim. Acta 65, 1971–1983. https://doi.org/10.1016/S0016-7037(01)00575-0.
Lafuente, B., Downs, R.T., Yang, H., Stone, N., 2016. The power of databases: the RRUFF project. In: Highlights in Mineralogical Crystallography, pp. 1–29. https://doi.org/10.1515/9783110417104-003.
Le Roux, G., Laverret, E., Shotyk, W., 2006. Fate of calcite, apatite and feldspars in an ombrotrophic peat bog, Black Forest, Germany. J. Geol. Soc. London 163, 641–646. https://doi.org/10.1144/0016-764920-035.
Liu, J., Yang, J., Cade-Menun, B.J., Hu, Y., Li, J., Peng, C., Ma, Y., 2017. Molecular speciation and transformation of soil legacy phosphorus with and without long-term phosphorus fertilization: insights from bulk and microprobe spectroscopy. Sci. Rep. 7, 15354. https://doi.org/10.1038/s41598-017-13498-7.
Lombi, E., Scheckel, K.G., Armstrong, R.D., Forrester, S., Cutler, J.N., Paterson, D., 2006. Speciation and distribution of phosphorus in a fertilized soil. Soil Sci. Soc. Am. J. 70, 2038–2048. https://doi.org/10.2136/sssaj2006.0051.
Lu, S., Shao, L., Wu, M., Jiao, Z., 2006. Mineralogical characterization of airborne individual particulates in Beijing PM_{10}. J. Environ. Sci. 18, 90–95.
MacDonald, G., 1949. Petrography of the Island of Hawaii in: United States Geological Survey, Professional Paper 214-D.
Melrose, J., Perroy, R., Cares, S., 2015. Statewide Agricultural Land Use Baseline 2015. Hilo, Hawaii.
Merrill, J.T., Uematsu, M., Bleck, R., 1989. Meteorological analysis of long range transport of mineral aerosols over the North Pacific. J. Geophys. Res. [Atmos.] 94, 8584–8598. https://doi.org/10.1029/JD094iD06p08584.
Nakai, S., Halliday, A.N., Rea, D.K., 1993. Provenance of dust in the Pacific Ocean. Earth Planet. Sci. Lett. 119, 143–157. https://doi.org/10.1016/0012-821X(93)90012-X.
Okin, G.S., Mahowald, N., Chadwick, O.A., Artaxo, P., 2004. Impact of desert dust on the biogeochemistry of phosphorus in terrestrial ecosystems. Global Biogeochem. Cycles 18. https://doi.org/10.1029/2003gb002145.
Peay, K.G., von Sperber, C., Cardarelli, E., Toju, H., Francis, C.A., Chadwick, O.A., Vitousek, P.M., 2017. Convergence and contrast in the community structure of Bacteria, Fungi and Archaea along a tropical elevation–climate gradient. FEMS Microbiol. Ecol. 93. https://doi.org/10.1093/femsec/fix045.
Porder, S., Hilley, G.E., Chadwick, O.A., 2007. Chemical weathering, mass loss, and dust inputs across a climate by time matrix in the Hawaiian Islands. Earth Planet. Sci. Lett. 258, 414–427. https://doi.org/10.1016/j.epsl.2007.03.047.
Pribyl, D.W., 2010. A critical review of the conventional SOC to SOM conversion factor. Geoderma 156, 75–83. https://doi.org/10.1016/j.geoderma.2010.02.003.
Prietzel, J., Dümig, A., Wu, Y., Zhou, J., Klysubun, W., 2013. Synchrotron-based P K-edge XANES spectroscopy reveals rapid changes of phosphorus speciation in the topsoil of two glacier foreland chronosequences. Geochim. Cosmochim. Acta 108, 154–171. https://doi.org/10.1016/j.gca.2013.01.029.
Prietzel, J., Klysubun, W., 2018. Phosphorus K-edge XANES spectroscopy has probably often underestimated iron oxyhydroxide-bound P in soils. J. Synchrotron Radiat. 25, 1736–1744. https://doi.org/10.1107/S1600577518013334.
Pye, K., Zhou, L.-P., 1989. Late Pleistocene and Holocene aeolian dust deposition in North China and the Northwest Pacific Ocean. Palaeogeogr. Palaeoclimatol. Palaeoecol. 73, 11–23. https://doi.org/10.1016/0031-0182(89)90041-2.
Ravel, B., Newville, M., 2005. ATHENA, ARTEMIS, HEPHAESTUS: data analysis for X-ray absorption spectroscopy using IFEFFIT. J. Synchrotron Radiat. 12, 537–541. https://doi.org/10.1107/S0909049505012719.
Rea, D.K., 1994. The paleoclimatic record provided by eolian deposition in the deep sea: the geologic history of wind. Rev. Geophys. 32, 159–195. https://doi.org/10.1029/93RG03257.
Rex, R.W., Syers, J.K., Jackson, M.L., Clayton, R.N., 1969. Eolian Origin of Quartz in Soils of Hawaiian Islands and in Pacific Pelagic Sediments. Science (80-.) 163https://doi.org/10.1126/science.163.3864.277. 277 LP – 279.
Rivard, C., Lanson, B., Cotte, M., 2016. Phosphorus speciation and micro-scale spatial distribution in North-American temperate agricultural soils from micro X-ray fluorescence and X-ray absorption near-edge spectroscopy. Plant Soil 401, 7–22. https://doi.org/10.1007/s11104-015-2494-5.
Sansone, F.J., Benitez-Nelson, C.R., Resing, J.A., DeCarlo, E.H., Vink, S.M., Heath, J.A., Huebert, B.J., 2002. Geochemistry of atmospheric aerosols generated from lava-seawater interactions. Geophys. Res. Lett. 29, 44–49. https://doi.org/10.1029/2001GL013882.
Schaefers, F., Mertin, M., Gorgoi, M., 2007. KMC-1: a high resolution and high flux soft x-ray beamline at BESSY. Rev. Sci. Instrum. 78, 123102. https://doi.org/10.1063/1.2808334.
Siegenthaler, M.B., Tamburini, F., Frossard, E., Chadwick, O., Vitousek, P., Pistocchi, C., Mészáros, É., Helfenstein, J., 2020. A dual isotopic (32P and 18O) incubation study to disentangle mechanisms controlling phosphorus cycling in soils from a climatic gradient (Kohala, Hawaii). Soil Biol. Biochem. 107920. https://doi.org/10.1016/j.soilbio.2020.107920.
Slessarev, E.W., Lin, Y., Bingham, N.L., Johnson, J.E., Dai, Y., Schimel, J.P., Chadwick, O.A., 2016. Water balance creates a threshold in soil pH at the global scale. Nature 540, 567–569. https://doi.org/10.1038/nature20139.
Solé, V.A., Papillon, E., Cotte, M., Walter, P., Susini, S., 2007. A multiplatform code for the analysis of energy-dispersive X-ray fluorescence spectra. Spectrochim. Acta B 62, 63–68. https://doi.org/10.1016/j.sab.2006.12.002.
Sprenger, M., Wernli, H., 2015. The LAGRANTO Lagrangian analysis tool – version 2.0. Geosci. Model Dev. 8, 2569–2586. https://doi.org/10.5194/gmd-8-2569-2015.
Stockdale, A., Krom, M.D., Mortimer, R.J.G., Benning, L.G., Carslaw, K.S., Herbert, R.J., Shi, Z., Myriokefalitakis, S., Kanakidou, M., Nenes, A., 2016. Understanding the nature of atmospheric acid processing of mineral dusts in supplying bioavailable phosphorus to the oceans. Proc. Natl. Acad. Sci. 113, 14639–14644. https://doi.org/10.1073/pnas.1608136113.
Swap, R., Garstang, M., Greco, S., Talbot, R., Kallberg, P., 1992. Saharan dust in the Amazon Basin. Tellus B 44, 133–149. https://doi.org/10.1034/j.1600-0889.1992.t01-1-00005.x.
Tamburini, F., Pfahler, V., Bünemann, E.K., Guelland, K., Bernasconi, S.M., Frossard, E., 2012. Oxygen isotopes unravel the role of microorganisms in phosphate cycling in soils. Environ. Sci. Technol. 46, 5956–5962. https://doi.org/10.1021/es300311h.
Tipping, E., Benham, S., Boyle, J.F., Crow, P., Davies, J., Fischer, U., Guyatt, H., Helliwell, R., Jackson-Blake, L., Lawlor, A.J., Monteith, D.T., Rowe, E.C., Toberman, H., 2014. Atmospheric deposition of phosphorus to land and freshwater. Environ. Sci. Process. Impacts 16, 1608–1617. https://doi.org/10.1039/c3em00641g.
Tsamalis, C., Chédin, A., Pelon, J., Capelle, V., 2013. The seasonal vertical distribution of the Saharan Air Layer and its modulation by the wind. Atmos. Chem. Phys. 13, 11235–11257. https://doi.org/10.5194/acp-13-11235-2013.
van der Does, M., Knippertz, P., Zschenderlein, P., Giles Harrison, R., Stuut, J.-B.W., 2018. The mysterious long-range transport of giant mineral dust particles. Sci. Adv. 4, eaau2768. https://doi.org/10.1126/sciadv.aau2768.
Vantelon, D., Trcera, N., Roy, D., Moreno, T., Mailly, D., Guilet, S., Metchalkov, E., Delmotte, F., Lassalle, B., Lagarde, P., Flank, A.-M., 2016. The LUCIA beamline at SOLEIL. J. Synchrotron Radiat. 23, 635–640. https://doi.org/10.1107/S1600577516000746.
Vitousek, P.M., Chadwick, O.A., 2013. Pedogenic thresholds and soil process domains in basalt-derived soils. Ecosystems 16, 1379–1395. https://doi.org/10.1007/s10021-013-9690-z.
Vogel, C., Adam, C., Sekine, R., Schiller, T., Lipiec, E., McNaughton, D., 2013. Determination of phosphorus fertilizer soil reactions by Raman and synchrotron infrared microspectroscopy. Appl. Spectrosc. 67 (10), 1165–1170.
Vogel, C., Rivard, C., Tanabe, I., Adam, C., 2016. Microspectroscopy – promising techniques to characterize phosphorus in soil. Commun. Soil Sci. Plant Anal. 47 (18), 2088–2102. https://doi.org/10.1080/00103624.2016.1228942.
Vogel, C., Rivard, C., Wilken, V., Muskolus, A., Adam, C., 2018. Performance of secondary P-fertilizers in pot experiments analyzed by phosphorus X-ray absorption near-edge structure (XANES) spectroscopy. Ambio 47, 62–72. https://doi.org/10.1007/s13280-017-0973-z.
Walker, T.W., Syers, J.K., 1976. The fate of phosphorus during pedogenesis. Geoderma 15, 1–19. https://doi.org/10.1016/0016-7061(76)90066-5.
Wang, R., Balkanski, Y., Boucher, O., Ciais, P., Peñuelas, J., Tao, S., 2015. Significant contribution of combustion-related emissions to the atmospheric phosphorus budget. Nat. Geosci. 8, 48–54. https://doi.org/10.1038/ngeo2324.
Webb, S.M., 2011. The MicroAnalysis Toolkit: X-ray Fluorescence Image Processing Software. In: Amer. Inst. Phys. Conf. Proc. 1365196-1365199. https://aip.scitation.org/doi/abs/10.1063/1.3625338.
Werner, F., Mueller, C.W., Thieme, J., Gianoncelli, A., Rivard, C., Höschen, C., Prietzel, J.,

2017. Micro-scale heterogeneity of soil phosphorus depends on soil substrate and depth. Sci. Rep. 7, 3203. https://doi.org/10.1038/s41598-017-03537-8.
Westheimer, F.H., 1987. Why nature chose phosphates. Science (80-.) 235, 1173.
Wiacek, A., Peter, T., Lohmann, U., 2010. The potential influence of Asian and African mineral dust on ice, mixed-phase and liquid water clouds. Atmos. Chem. Phys. 10, 8649–8667. https://doi.org/10.5194/acp-10-8649-2010.
Xiong, W., Peng, J., Hu, Y., 2012. Use of X-ray absorption near edge structure (XANES) to identify physisorption and chemisorption of phosphate onto ferrihydrite-modified diatomite. J. Colloids Interface Sci. 368, 528–532. https://doi.org/10.1016/j.jcis.2011.11.041.
Yang, X., Post, W.M., Thornton, P.E., Jain, A., 2013. The distribution of soil phosphorus for global biogeochemical modeling. Biogeosciences 10, 2525–2537. https://doi.org/10.5194/bg-10-2525-2013.
Ziegler, K., Hsieh, J.C.C., Chadwick, O.A., Kelly, E.F., Hendricks, D.M., Savine, S.M., 2003. Halloysite as a kinetically controlled end product of arid-zone basalt weathering. Chem. Geol. 202, 461–478. https://doi.org/10.1016/j.chemgeo.2002.06.001.